nature physics

ARTICLES

PUBLISHED ONLINE: 8 MAY 2011 | DOI: 10.1038/NPHYS1994

Noise spectroscopy through dynamical decoupling with a superconducting flux qubit

Jonas Bylander[1]*, Simon Gustavsson[1], Fei Yan[2], Fumiki Yoshihara[3], Khalil Harrabi[3]†, George Fitch[4], David G. Cory[2,5,6], Yasunobu Nakamura[3,7], Jaw-Shen Tsai[3,7] and William D. Oliver[1,4]

Quantum coherence in natural and artificial spin systems is fundamental to applications ranging from quantum information science to magnetic-resonance imaging and identification. Several multipulse control sequences targeting generalized noise models have been developed to extend coherence by dynamically decoupling a spin system from its noisy environment. In any particular implementation, however, the efficacy of these methods is sensitive to the specific frequency distribution of the noise, suggesting that these same pulse sequences could also be used to probe the noise spectrum directly. Here we demonstrate noise spectroscopy by means of dynamical decoupling using a superconducting qubit with energy-relaxation time $T_1 = 12\,\mu s$. We first demonstrate that dynamical decoupling improves the coherence time T_2 in this system up to the $T_2 = 2\,T_1$ limit (pure dephasing times exceeding 100 μs), and then leverage its filtering properties to probe the environmental noise over a frequency (f) range 0.2–20 MHz, observing a $1/f^{\alpha}$ distribution with $\alpha < 1$. The characterization of environmental noise has broad utility for spin-resonance applications, enabling the design of optimized coherent-control methods, promoting device and materials engineering, and generally improving coherence.

Decoherence of a quantum superposition state in natural and artificial two-level spin systems arises from the interaction between the constituent system and the uncontrolled degrees of freedom in its environment. Within the standard Bloch–Redfield picture of two-level system dynamics, decoherence is characterized by two rates: a longitudinal relaxation rate $\Gamma_1 = 1/T_1$ due to the exchange of energy with the environment, and a transverse relaxation rate $\Gamma_2 = \Gamma_1/2 + \Gamma_\varphi$, which contains the pure dephasing rate Γ_φ. Irreversible energy relaxation can only be mitigated by reducing the amount of environmental noise, by reducing the qubit's internal sensitivity to that noise, or through multiqubit encoding and error-correction protocols (which already presume ultralow error rates). In contrast, dephasing is in principle reversible and can be refocused dynamically through the application of coherent control-pulse methods.

Since the 1950s, several single-[1] and multipulse[2–4] sequences have been developed within the field of nuclear magnetic resonance[4] and later extended to electron spin resonance. More recently, such dynamical-decoupling techniques have been applied to mitigate noise and extend coherence in qubits based on atomic ensembles[5–7] and single atoms[8], spin ensembles[9], semiconductor quantum dots[10,11] and diamond nitrogen–vacancy centres[12,13]. In most experimental[5–13] and theoretical[14–20] dynamical-decoupling works, the focus has been on using pulse sequences to minimize errors (that is, extend T_2) within an operating time τ such that $\tau \ll T_2$, for example, to reach fault-tolerant error thresholds.

We extend multipulse dynamical decoupling to superconducting qubits[21]. However, our interest here is more general. Our goal is to measure the environmental noise spectrum[19,22], which we accomplish by monitoring the response of the spin to its environment, as mediated by dynamical-decoupling pulses, over a range of times that extends from the small-error limit ($\tau \ll T_2$) to the large-error limit ($\tau \sim T_2$). This should not be viewed as unique to our purpose; indeed, applications such as magnetic resonance imaging and sensing generally operate in the presence of large errors with variability from sample to sample such that there is probably no generally optimal pulse sequence[23]. In these cases, characterizing the noise-power spectral density (PSD) precisely would greatly facilitate the design of tailored pulse sequences[4,14] that can reduce error rates, reduce the pulse number or power required to achieve a given error rate and otherwise engineer an improved measurement outcome.

In our test system, a superconducting (persistent-current) flux qubit[24,25], we carry out noise spectroscopy by dynamical decoupling over the wide frequency range 0.2–20 MHz: the obtained noise PSD is a $1/f^{\alpha}$ power-law with $\alpha \approx 0.9$. We independently confirm this noise PSD with that obtained from a Rabi-spectroscopy approach and, for completeness, characterize the high-frequency PSD over the range 5.4–21 GHz by monitoring the qubit's energy-relaxation rate[26].

The device (Fig. 1a, Supplementary Fig. S1) is an aluminium loop interrupted by four Al–AlO_x–Al Josephson junctions. When an external magnetic flux Φ threading the loop is close to half a superconducting flux quantum $\Phi_0/2$, the diabatic states correspond to clockwise and anticlockwise persistent currents $I_p = 0.18\,\mu A$ with energies $\pm\hbar\varepsilon/2 = \pm I_p \Phi_b$, tunable by the flux bias $\Phi_b = \Phi - \Phi_0/2$. At $\Phi_b = 0$, the degenerate persistent-current states hybridize with a strength $\hbar\Delta = h \times 5.3662\,GHz$ (Fig. 1b, Supplementary Fig. S2b),

[1]Research Laboratory of Electronics, Massachusetts Institute of Technology, Cambridge, Massachusetts 02139, USA, [2]Department of Nuclear Science and Engineering, Massachusetts Institute of Technology, Cambridge, Massachusetts 02139, USA, [3]The Institute of Physical and Chemical Research (RIKEN), Wako, Saitama 351-0198, Japan, [4]MIT Lincoln Laboratory, 244 Wood Street, Lexington, Massachusetts 02420, USA, [5]Institute for Quantum Computing and Department of Chemistry, University of Waterloo, Ontario, N2L 3G1, Canada, [6]Perimeter Institute for Theoretical Physics, Waterloo, Ontario, N2J 2W9, Canada, [7]Green Innovation Research Laboratories, NEC Corporation, Tsukuba, Ibaraki 305-8501, Japan. †Present address: Physics Department, King Fahd University of Petroleum & Minerals, Dhahran 31261, Saudi Arabia. *e-mail: bylander@mit.edu.

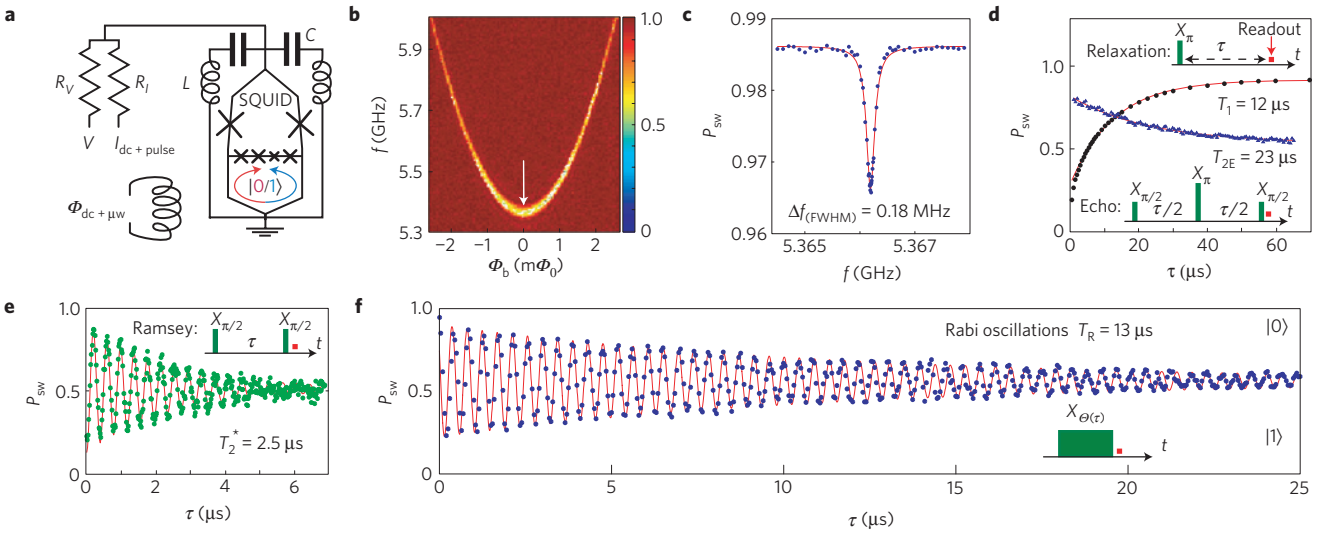

Figure 1 | Qubit device and characterization. a, Device and biasing schematic representation: an aluminium superconducting loop interrupted by Josephson junctions (crosses) with a readout d.c. SQUID. **b**, Frequency spectroscopy of the qubit's $|0\rangle \rightarrow |1\rangle$ transition. **c**, Spectroscopy at $\Phi_b = 0$ (arrow in **b**). **d**, Echo decay (blue triangles) and relaxation from the excited state (black circles) at $\Phi_b = 0$. In the insets, τ is a time delay and X_Θ symbolizes a rotation of the Bloch vector by the angle Θ around the axis $\hat{\sigma}_x$. The red squares indicate the readout. **e**, Free-induction decay (Ramsey fringe) at $\Phi_b = 0$. **f**, Rabi oscillations at $\Phi_b = 0$.

where $\hbar = h/2\pi$ and h is Planck's constant. The corresponding two-level Hamiltonian is

$$\hat{\mathcal{H}} = -\frac{\hbar}{2}[(\varepsilon + \delta\varepsilon)\hat{\sigma}_x + (\Delta + \delta\Delta)\hat{\sigma}_z] \qquad (1)$$

which includes noise fluctuation terms $\delta\varepsilon$ and $\delta\Delta$, and $\hat{\sigma}_{x,z}$ are Pauli operators. The ground ($|0\rangle$) and excited ($|1\rangle$) states have frequency splitting $\omega_{01} = \sqrt{\varepsilon^2 + \Delta^2}$ and are well isolated owing to the qubit's large anharmonicity, $\omega_{12}/\omega_{01} \approx 5$. Noise and decoherence in superconducting qubits have been studied theoretically[27–30] and experimentally[26,29,31]. In our qubit, the environmental noise leading to fluctuations $\delta\varepsilon$ (for example, flux noise) and $\delta\Delta$ (for example, critical current and charge noise) physically couples to the qubit in the ε–Δ frame (equation (1)). However, their manifestation as longitudinal noise (dephasing) or transverse noise (energy relaxation) is tunable[29] by the flux bias Φ_b and determined, respectively, by their projections $\delta\omega_{z'}$ onto the qubit's quantization axis $\hat{\sigma}_{z'}$ (which makes an angle $\theta = \arctan(\varepsilon/\Delta)$ with $\hat{\sigma}_z$) and $\delta\omega_{\perp'}$ onto the plane perpendicular to $\hat{\sigma}_{z'}$.

The chip is mounted in a ^{3}He/^{4}He dilution refrigerator with 12 mK base temperature. For each experimental trial, we initialize the qubit by waiting sufficient time (~ 1 ms) for it to relax to its ground state. We drive the desired quantum-state rotations of angle Θ by applying calibrated in-phase (X_Θ) and quadrature (Y_Θ) harmonic flux pulses to the qubit loop. The pulses consist of Gaussian envelopes with a typical standard deviation $\sigma = 1.2$ ns and truncated at $\pm 3\sigma$. The qubit readout has 79% visibility (Supplementary Fig. S3) and is carried out in the energy basis by determining the switching probability P_{sw} of a hysteretic dc SQUID, averaging over several thousand trials (see Supplementary Information C).

We begin with a spectroscopic characterization of our device in the absence of multipulse dynamical decoupling. The qubit level splitting ω_{01} is measured through saturated frequency spectroscopy (Fig. 1b), and at low power it exhibits a Lorentzian full-width-at-half-maximum linewidth $\Delta f_{(FWHM)} = 0.18$ MHz at $\Phi_b = 0$ (Fig. 1c). The energy relaxation is generally exponential and its time constant $T_1 = 12 \pm 1$ μs (Fig. 1d) is remarkably long among superconducting qubits[21], about six times longer than a similarly designed and fabricated device[31]. We observe very long decay times at $\Phi_b = 0$ for the Hahn spin echo, $T_{2E} = 23$ μs (Fig. 1d), Ramsey free induction, $T_2^* = 2.5$ μs (Fig. 1e) and Rabi oscillations, $T_R = 13$ μs (Fig. 1f). The dephasing times decrease (rates increase) dramatically away from $\Phi_b = 0$ owing to the qubit's increased sensitivity $|\partial\omega_{01}/\partial\varepsilon|$ to the dominant $\delta\varepsilon$-noise (flux noise) in this system[31]. Furthermore, although the spin echo and Rabi oscillations exhibit an essentially T_1-limited, exponential decay at $\Phi_b = 0$, in general their noise-dependent decay functions are non-exponential, indicating noise sources with long correlation times, singular near $\omega \approx 0$ (for example, $1/f$-type noise at low frequencies, relevant to dephasing).

The frequency distribution of the noise power for a noise source λ that leads to decoherence is characterized by its PSD $S_\lambda(\omega) = (1/2\pi)\int_{-\infty}^{\infty} dt\, \langle\lambda(0)\lambda(t)\rangle \exp(-i\omega t)$. A superposition state's accumulated phase $\varphi(t) = \langle\omega_{01}\rangle t + \delta\varphi(t)$ diffuses owing to adiabatic fluctuations of the transition frequency, $\delta\varphi(t) = (\partial\omega_{01}/\partial\lambda)\int_0^t dt'\delta\lambda(t')$, where $\partial\omega_{01}/\partial\lambda$ is the qubit's longitudinal sensitivity to λ-noise. For noise generated by a large number of fluctuators that are weakly coupled to the qubit, the statistics are Gaussian. Ensemble averaging over all realizations of the stochastic process $\delta\lambda(t)$, the dephasing is $\langle\exp[i\,\delta\varphi(t)]\rangle \equiv \exp[-\chi_N(t)]$, with the coherence integral

$$\chi_N(\tau) = \tau^2 \sum_\lambda \left(\frac{\partial\omega_{01}}{\partial\lambda}\right)^2 \int_0^\infty d\omega\, S_\lambda(\omega)\, g_N(\omega,\tau) \qquad (2)$$

where τ is the free evolution time, N will denote the number of π-pulses in the pulse sequences[5,17] and g_N is a dimensionless weighting function defined in equation (3).

The function $g_N(\omega,\tau)$ can be viewed as a frequency-domain filter of the noise $S_\lambda(\omega)$. Its filter properties depend on the number N and distribution of π-pulses[5,6,17,19,32],

$$g_N(\omega,\tau) = \frac{1}{(\omega\tau)^2}\left|1 + (-1)^{1+N}\exp(i\omega\tau) + 2\sum_{j=1}^{N}(-1)^j \exp(i\omega\delta_j\tau)\cos(\omega\tau_\pi/2)\right|^2 \qquad (3)$$

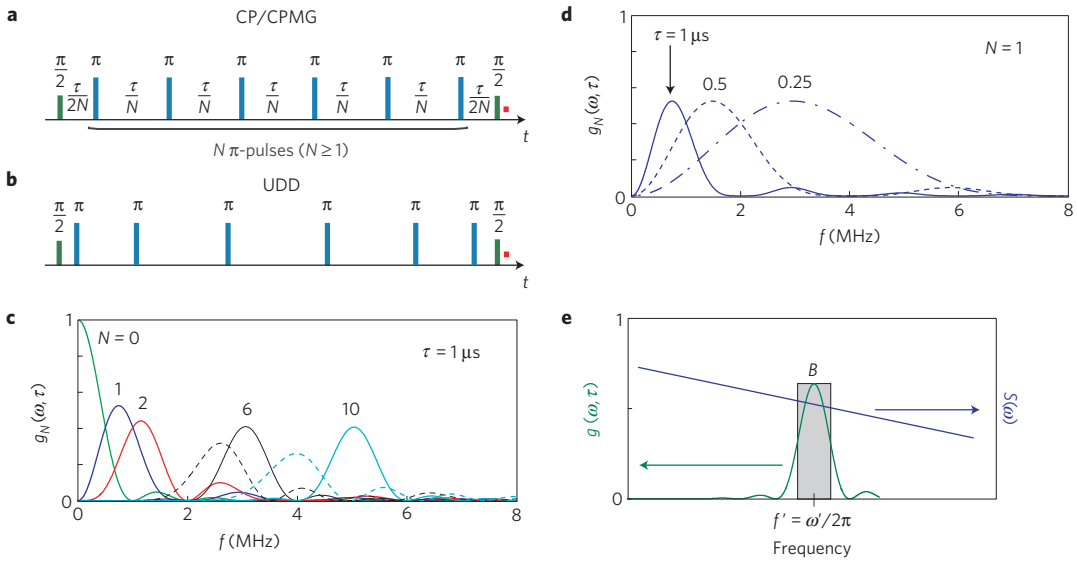

Figure 2 | Dynamical-decoupling pulse sequences. a, Schematic representation of the CP(MG) sequence; the π-pulses are shifted 0° (X_π) and 90° (Y_π) from the π/2-pulses ($X_{\pi/2}$) for CP and CPMG, respectively. **b**, The Nth UDD pulse (Y_π) has the relative position $\delta_j = \sin^2(\pi j/(2N+2))$. **c**, CP(MG) (solid lines) and UDD (dashed) filter functions $g_N(\omega,\tau)$, equation (3), for a total pulse-sequence length $\tau = 1\,\mu$s (identical for $N = 0,1,2$). **d**, Single-π-pulse ($N = 1$) filter function for various total pulse lengths τ. **e**, An illustration using the filter function $g_N(\omega,\tau)$ to sample the noise PSD for a particular N and τ corresponding to an angular frequency ω'. $S(\omega)$ is assumed constant within the filter's bandwidth B.

where $\delta_j \in [0,1]$ is the normalized position of the centre of the jth π-pulse between the two π/2-pulses, τ is the total free-induction time and τ_π is the length of each π-pulse[5,6], yielding a total sequence length $\tau + N\tau_\pi$. As the number of pulses increases for fixed τ, the filter function's peak shifts to higher frequencies (Fig. 2c), leading to a reduction in the net integrated noise (equation (2)) for $1/f^\alpha$-type noise spectra with $\alpha > 0$. Additionally, for a fixed time separation $\tau' = \tau/N$ (valid for $N \geq 1$), the filter sharpens and asymptotically peaks at $\omega'/2\pi = 1/2\tau'$ as more pulses are added. In principle, we can adapt the filter function to suit a particular noise spectrum through the choice of dynamical-decoupling protocol. Note that we have purposefully written $g_N(\omega,\tau)$ as a band-pass filter (Fig. 2c–e), which we will effectively use to sample the environmental noise $S_\lambda(\omega)$ by varying the number of pulses N and the total sequence time τ. This interpretation can be contrasted with several previous works[5,6,17–19], in which the quantity $(\omega\tau)^2 g_N(\omega,\tau)$ was interpreted as a high-pass filter acting on a phase noise $S_\lambda(\omega)/\omega^2$ (see Supplementary Information H).

The effect of the band-pass filter function is clearly manifest in the Ramsey free-induction and Hahn spin-echo decay rates and their flux-bias dependence (Fig. 3a), both of which are apparently consistent with Gaussian-distributed, $1/f$-type noise[29]. Ramsey free induction, the free evolution of a superposition state for a time τ (Fig. 2a with no π-pulses), has a filter function g_0 peaked at $\omega = 0$ (Fig. 2c) and is sensitive to low-frequency longitudinal noise $\delta\omega_{z'}(\omega \to 0)$. Inhomogeneities in the precession frequency ω_{01} from one realization of the pulse sequence to the next lead to a decay of the averaged signal. Following convention, we denote such fluctuations 'quasi-static' noise and characterize them by a noise variance σ_λ^2; see Table 1. In contrast, the Hahn spin-echo sequence[1], a single π-pulse applied at time $\tau/2$ (Fig. 2a with one π-pulse), has a filter function g_1 peaked away from $\omega = 0$ (Fig. 2c) and is less sensitive to quasi-static noise. We plot the decay rates $1/T_e$ versus flux bias Φ_b for Ramsey and echo data in Fig. 3a, where, for purposes of comparison amongst different decay envelopes, T_e parameterizes the time T_2 to decay by a factor $1/e$ independent of the exact decay function. At $\Phi_b = 0$, $\delta\Delta$-noise is the dominant longitudinal noise that limits the Ramsey decay, yet it is refocused with a single π-pulse resulting in the T_1-limited exponential echo decay in Fig. 1d. As $|\Phi_b|$ is increased, both the Ramsey and echo decay rates increase owing to the qubit's increased longitudinal sensitivity to $\delta\varepsilon$-noise (see Fig. 3a, and Supplementary Information E and Fig. S4). The $\delta\varepsilon$-noise becomes too large for the echo to refocus efficiently, owing to its high-frequency tail. We find best-fit phase-decay functions that are Gaussian, $\chi(\tau) = (\Gamma_{\varphi,\mathrm{F(E)}}\,\tau)^2$, and extract the ratio $\Gamma_{\varphi,\mathrm{F}}(\Phi_b)/\Gamma_{\varphi,\mathrm{E}}(\Phi_b) \approx 4.5$; both findings are as expected for $1/f$ noise[29]. The equivalent flux-noise amplitude[31] is $A_\Phi = (1.7\,\mu\,\Phi_0)^2$. Importantly, we note that, in this analysis and related works[29,31], the PSD was presumed *a priori* to take the form $1/f^\alpha$ with $\alpha = 1$ and no detailed information regarding the actual noise frequency distribution is extracted.

Numerical simulations (see Supplementary Information F), including the measured T_1 decay at each Φ_b, linearly coupled and uncorrelated quasi-static noises, and uncorrelated dynamic $1/f$ noise from 10^4 to 10^{10} Hz, reproduce the entire Φ_b-dependence of T_2^* and T_{2E} using the parameters in Table 1 and are also consistent with equation (2).

To extend the filter function to higher frequencies, we evaluated three different multipulse dynamical-decoupling protocols relevant for $1/f$-type power-law noise spectra[15,16,20]. The CP and CPMG sequences[2,3] (after Carr, Purcell, Meiboom and Gill; Fig. 2a) are multipulse extensions of the Hahn echo with equally spaced π-pulses whose phases differ from the initial π/2-pulse by 0° (X_π) and 90° (Y_π), respectively. The UDD sequence[17] (Uhrig dynamical decoupling; Fig. 2b) has Y_π-pulse positions defined by $\delta_j = \sin^2(\pi j/(2N+2))$ and, therefore, has a distinct filter function (Fig. 2c).

In Fig. 3a, we include the $1/T_e$ decay rates for CPMG dynamical-decoupling sequences with $N = 2\ldots48$ π-pulses along with the Ramsey ($N = 0$) and Hahn-echo ($N = 1$) data already discussed. Although the qubit's sensitivity to $\delta\varepsilon$ (flux) noise grows with increasing $|\Phi_b|$, the decay rates monotonically improve towards the $1/2T_1$ limit when the number of π-pulses increases, extending the range around $\Phi_b = 0$ for which pure dephasing is negligible. We explicitly demonstrate this improvement in detail for each N up to $\varepsilon/2\pi = 400$ MHz, corresponding to a change in qubit frequency of 15 MHz. The dynamical-decoupling method is not fundamentally limited to this range, however. For example, we

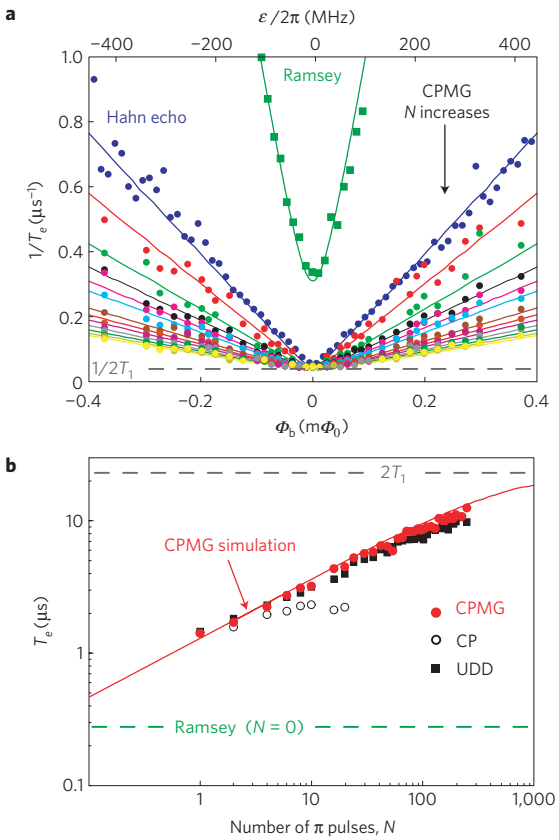

Figure 3 | Dephasing under the CPMG sequence. a, Decay rates (inverse of 1/*e* times) versus flux detuning: free induction (Ramsey, $N=0$, green squares) and CPMG (coloured circles) with $N=1$, 2, 4, 6, 8, 10, 16, 20, 24, 30, 36, 42, 48 (colours correspond to those in Fig. 2c). Solid lines are calculations using equation (2) with parameters in Table 1. **b**, 1/*e* decay time under *N*-pulse CPMG, CP and UDD sequences at $\Phi_b=-0.4\,m\Phi_0$ ($\varepsilon/2\pi=430$ MHz). The simulation (red line) assumes ideal pulses and noise acting during the free evolution.

observe a coherence improvement going from $N=1$ to $N=2$ π-pulses beyond $\varepsilon/2\pi=6.4$ GHz, corresponding to a qubit frequency of $\omega_{01}/2\pi>8.4$ GHz (see Supplementary Fig. S5). Although the coherence times generally decrease as $|\varepsilon|$ is increased owing to the qubit's increased sensitivity to flux noise, the fractional improvement in coherence is essentially constant over the entire range. The echo-decay time T_{2E} remains considerably longer than the π-pulse time τ_π, indicating that the refocusing remains efficient.

At a specific flux bias $\Phi_b=-0.4\,m\Phi_0$, where the qubit is highly sensitive to $\delta\varepsilon$ noise, the CPMG sequence gives a marked improvement in the decay time T_e up to $N\approx200$ π-pulses, beyond which pulse errors begin to limit the CPMG efficiency (Fig. 3b). We achieve a 50-fold enhancement of T_2^{CPMG} over the Ramsey T_2^*, and a well over 100-fold improvement in the Gaussian pure dephasing time T_φ. The CPMG sequence performs about 5% better than UDD, indicating that the $1/f$ $\delta\varepsilon$-noise spectrum exhibits a relatively soft (if any) high-frequency cutoff[19,20], because the UDD filter function has larger side-lobes at higher frequencies (Fig. 2c). CPMG also dramatically outperforms CP, despite having the same filter function, as Y_π-pulse errors appear only to fourth order with CPMG, whereas with CP X_π errors accumulate to second order[33].

Given its superior performance mitigating noise, we in turn use the filtering property of the CPMG sequence to characterize the flux-noise ($\delta\varepsilon$) spectrum. The filter $g_N(\omega,\tau)$ is sufficiently narrow about ω' that we can treat the noise as constant within its bandwidth B and approximate equation (2) as $\chi_N(\tau)\approx\tau^2(\partial\omega_{01}/\partial\varepsilon)^2S_\varepsilon(\omega')g_N(\omega',\tau')B$ (Fig. 2e). We compute ω' and B numerically for each N and τ used in the CPMG measurements of Fig. 3b. The measured decay function contains three decay rates: dephasing $\Gamma_\varphi^{(N)}$ and exponential relaxation $\Gamma_1/2$ during the total free-evolution time τ, and pulse-induced decay Γ_p during $N\tau_\pi$. Using a recursive method explained in detail in part I of Supplementary Information, we effectively divide out the Γ_1 and Γ_p components from the raw data and compute the noise PSD $S_\varepsilon(\omega)$ without presuming a functional form for the decay functions or the spectrum. This procedure yields a $1/f^\alpha$-type PSD $S_\varepsilon(\omega)$ over the region 0.2–20 MHz in Fig. 5, with a slight increase in the measured PSD above 2 MHz. Interestingly, by fitting the lower-frequency, linear portion we find that the PSD is approximated by a $1/f^\alpha$ power law[34] with $\alpha\approx0.9$ (solid, red line) and noise amplitude $A_\Phi=(0.8\mu\Phi_0)^2$.

To check the noise-spectroscopy results we analysed the decoherence during driven evolution[29,35] (see Supplementary Information J for details). A transverse driving field at frequency ω and drive strength Ω results in Rabi oscillations with angular nutation frequency $\Omega_R=\sqrt{\Omega^2+(\Delta\omega)^2}\approx\Omega+(\Delta\omega)^2/2\Omega$, where $\Delta\omega=\omega-\omega_{01}$. The noise at the Rabi frequency, $\Gamma_\Omega^{(\lambda)}=\pi S_\lambda(\Omega_R)$, along with T_1 relaxation, comprises the usual exponential Rabi-decay rate

$$\Gamma_R=\left(\frac{3}{4}\Gamma_1+\frac{1}{2}\Gamma_\Omega^{(\Delta)}\right)\cos^2\theta+\left(\frac{\varepsilon}{\omega_{01}}\right)^2\frac{1}{2}\Gamma_\Omega^{(\varepsilon)} \qquad (4)$$

Table 1 | Coherence times and quasi-static noise parameters.

Noise parameters	$\sigma_\lambda/2\pi$	$\omega_{low}^\lambda/2\pi$	$\omega_{high}^\lambda/2\pi$	A_{Φ,i_c}
$\lambda=\varepsilon$ (equivalent Φ noise)	10 MHz	1 Hz	1 MHz	$(1.7\times10^{-6}\ \Phi_0)^2$
$\lambda=\Delta$ (equivalent i_c noise)	0.06 MHz	1 Hz	< 0.1 MHz	$(4.0\times10^{-6})^2$
Coherence times	T_1	T_2^*	T_2^{CPMG}	T_2^{CPMG}/T_2^*
$\Phi_b=0\,m\Phi_0$ ($\delta\Delta$ noise dominates)	12 μs	2.5 μs	23 μs ($N=1$)	9
$\Phi_b=-0.4\,m\Phi_0$ ($\delta\varepsilon$ noise dominates)	12 μs	0.27 μs	13 μs ($N=200$)	48

Coherence times and their improvement under dynamical decoupling at flux biases Φ_b where $\delta\varepsilon$ and $\delta\Delta$ noises dominate. Assuming that flux (Φ) and normalized critical current ($i_c=\delta I_c/I_c$) are responsible for all $\delta\varepsilon$ and $\delta\Delta$ noise, respectively, we convert these noises to frequency noise by the sensitivities $\kappa_\varepsilon=\partial\varepsilon/\partial\Phi=6.9\times10^9\ s^{-1}/m\Phi_0$ and $\kappa_\Delta=\partial\Delta/\partial i_c=20\times10^9\ s^{-1}$ (see Supplementary Information D). We then describe the quasi-static, Gaussian noise distributions by their standard deviations, σ_λ, obtained by integrating the noises $S_{\varepsilon,\Delta}(\omega)=\kappa_{\varepsilon,\Delta}^2A_{\Phi,ic}/\omega$ over the bandwidth given by the experimental protocol:

$$\sigma_\lambda^2=2\int_{\omega_{low}^\lambda}^{\omega_{high}^\lambda}d\omega\,S_\lambda(\omega).$$

The cutoff ω_{low}^λ is given by the averaging time over all trials, typically 1 s for 1,000 averages at 1 kHz repetition rate, and ω_{high}^λ by the typical free-evolution time, $\tau=1\,\mu s$, during a single trial. The noise strengths, A_{Φ,i_c}, are derived from the Ramsey and echo data, assuming a power law $1/f^{\alpha=1}$. These agree with previously reported values[31,39]. At $\varepsilon=0$, the dephasing improvement under a Hahn echo is greater than the theory would suggest; the lower ω_{high}^Δ gives consistency. Simulations using these parameters yield agreement with the Ramsey-fringe and Hahn-echo data (see Supplementary Information F), and they are consistent with equation (2).

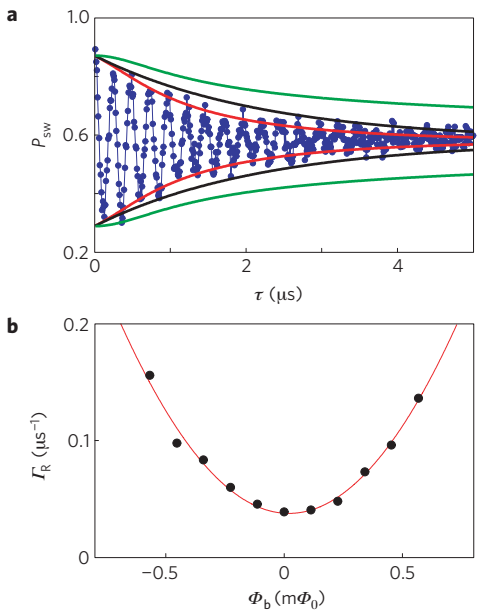

Figure 4 | Decoherence during driven dynamics. a, Rabi oscillations with $\Omega_R/2\pi = 2$ MHz at $\varepsilon/2\pi = 225$ MHz. The red line envelope is a fitting using $\zeta(t)$ and Γ_R. The black line shows the Γ_R decay only, and the green line the $\zeta(t)$-envelope contribution. **b**, Rabi-decay rate Γ_R versus flux detuning at $\Omega_R/2\pi = 2$ MHz, with a parabolic fit to equation (4) used to obtain $S_\varepsilon(\Omega_R) = (1/\pi)\,\Gamma_\Omega^{(\varepsilon)}$.

where $\cos^2\theta \approx 1$ as the quantization angle is small. In addition, accounting for the quasi-static noise with variance σ_ε^2 (Table 1), we obtain the decay function $\zeta(\tau) = (1 + (u\tau)^2)^{-1/4}$, where $u = (\varepsilon/\omega_{01})^2\,\sigma_\varepsilon^2/\Omega$. Figure 4a shows the combined decay function $\zeta(\tau) \times \exp(-\Gamma_R\tau)$.

To determine $S_\lambda(\Omega_R)$, we measured the Rabi oscillations versus Φ_b with fixed Rabi frequency Ω_R. For each Ω_R, we find the ε-independent part of the rate by fitting the envelope of the oscillations at $\varepsilon = 0$. The rate $\Gamma_\Omega^{(\Delta)}$ was too small to distinguish accurately from Γ_1, consistent with its correspondingly small quasi-static noise σ_Δ^2 (Table 1). Then, for $\varepsilon \neq 0$, we divide out the known quasi-static contribution $\zeta(\tau)$ and fit to the parabolic term in equation (4), from which we obtain $\Gamma_\Omega^{(\varepsilon)}$ (Fig. 4b). Using this approach, we find $S_\varepsilon(\Omega)$ to be consistent with the $1/f^\alpha$ noise obtained from the CPMG measurements (Fig. 5).

For completeness, we now turn to transverse noise at the qubit frequency ω_{01} responsible for energy relaxation Γ_1, that is, $\delta\varepsilon$-noise at $\varepsilon = 0$ and $\delta\Delta$-noise at $\varepsilon \gg \Delta$ (Fig. 5, inset). In the low-temperature limit, $k_B T \ll \hbar\omega_{01}$, where the environment cannot excite the qubit, the golden-rule expression for Γ_1 in a weakly damped quantum two-level system is

$$\Gamma_1 = \frac{\pi}{2}\sum_{\lambda\in\delta\varepsilon,\delta\Delta}\left(\frac{\partial\omega_{\perp'}}{\partial\lambda}\right)^2 S_\lambda(\omega_{01}) = \frac{\pi}{2}S(\omega_{01}) \qquad (5)$$

with $\partial\omega_{\perp'}/\partial\lambda$ the qubit's sensitivity to transverse noise and $S(\omega_{01})$ the total PSD (see Supplementary Information K).

We apply a long ($\gg T_1$) microwave pulse to saturate the transition and monitor the energy decay to the ground state, using equation (5) to determine $S(\omega_{01})$ over the frequency range $\Delta \leq \omega_{01} \leq 2\pi \times 21$ GHz by tuning Φ_b. At $\Phi_b = 0$ ($\omega_{01} = \Delta$) and using a measurement-repetition period $t_{rep} > 1$ ms, we observe $T_1 = 12 \pm 1$ μs as shown in Fig. 1d. As t_{rep} becomes shorter than 1 ms, the decay becomes increasingly non-exponential, which we attribute to the residual presence of non-equilibrium quasiparticles

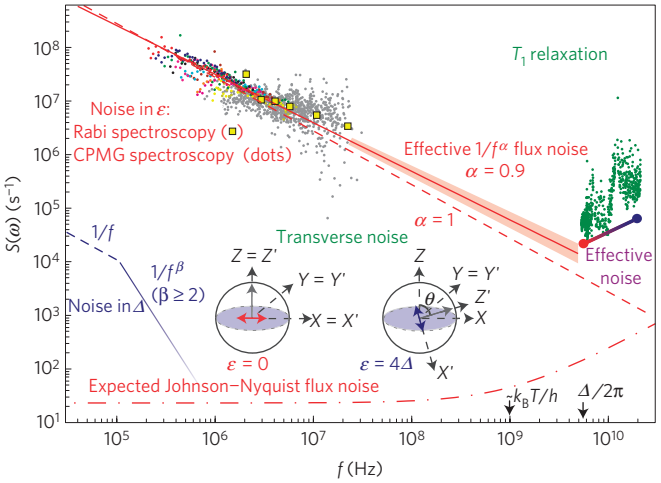

Figure 5 | Noise-power spectral density (PSD). Multicoloured dots, $\delta\varepsilon$-noise PSD (0.2–20 MHz) derived from CPMG data at $\Phi_b = -0.4\,m\Phi_0$ (see the text). Colours correspond to the various N in Fig. 3a; grey dots for data up to $N = 250$. Yellow squares, $\delta\varepsilon$-noise PSD (2–20 MHz) derived from Rabi spectroscopy (Fig. 4b and Supplementary Information J). Diagonal, dashed lines, Estimated flux (red) and $\delta\Delta$ (blue) $1/f$ noises, converted to frequency, inferred from the Ramsey and echo measurements (see A_{Φ,i_c} and ω_{high}^{Δ} in Table 1). Solid, red line, Power-law dependence, $S_\varepsilon(2\pi f) = \kappa_\varepsilon^2 A_\Phi/(2\pi f)^\alpha$, extrapolated beyond the qubit's frequency, $\Delta/2\pi$. Fitting the low-frequency, linear portion of the measured PSD derived from CPMG data (before the slight upturn beyond 2 MHz) yields the parameters $A_\Phi = (0.8\,\mu\Phi_0)^2$ and $\alpha = 0.9$ (see Supplementary Information I.3). The shaded area covers $\alpha \pm 0.05$. Green dots, High-frequency transverse noise is purely $\delta\varepsilon$-noise at $\Delta/2\pi = 5.4$ GHz and becomes predominantly $\delta\Delta$-noise at higher frequency. Purple line, Guide to indicate linearly increasing Nyquist (quantum) noise, including the eigenbasis rotation (see the inset); circles indicate transverse $\delta\varepsilon$- (red) and $\delta\Delta$- (blue) noises. Dash-dotted line, Expected thermal and quantum noise (equation (6)). Inset, Graphic representation of the quantization axis (grey arrows of fixed length) with the qubit's (Z') eigenstate tilted from the 'laboratory' frame (Z) by the angle θ. Fields $\varepsilon(\Phi_b)$ and Δ point in the X and Z directions, respectively. Red and blue double arrows indicate transverse noise.

generated by the switching SQUID during readout. We observe structure in the Γ_1-data due to environmental modes (for example cavity modes, impedance resonances) with uncontrolled couplings to the qubit (Fig. 5). For comparison, we plot the expected Johnson–Nyquist flux noise in Fig. 5 due to the $G = 1/50\,\Omega$ environment mutually coupled with strength $M = 0.02$ pH to the qubit through the microwave line,

$$S_\varepsilon^{JN}(\omega) = \frac{1}{2\pi}\left(\frac{\partial\varepsilon}{\partial\Phi}\right)^2 M^2\,\frac{2\hbar\omega\,G}{1 - e^{-\hbar\omega/k_B T}} \qquad (6)$$

This known noise source falls about 100 times below the measured PSD at $f_{01} = \Delta/2\pi$ (red circle in Fig. 5) where the relaxation is due solely to $\delta\varepsilon$-noise, indicating that the dominant source of energy relaxation lies elsewhere. Furthermore, the relaxation to a 300 Ω electrical environment through the measurement d.c. SQUID as estimated using a spin-boson model for the measured SQUID junction asymmetry in our device (<1%) is more than 100 times longer than observed[36]. The crossover f_c between the effective $1/f$- and f-type flux noises (Fig. 5) occurs near $k_B T/h$, where $T = 50$ mK is the approximate electronic temperature of our device[26,37]. Interestingly, projecting the $1/f^\alpha$ (longitudinal) flux noise from the CPMG measurements to higher frequencies comes within a factor of two of the (transverse) flux noise at frequency Δ; admittedly, however, α is not necessarily constant over the whole frequency spectrum.

The dynamical-decoupling protocols used in this work to carry out noise spectroscopy are the same sequences as used ubiquitously in spin-resonance applications to mitigate errors. By using the filtering property of these sequences, we have shown that it is possible to characterize directly the environmental-noise PSD, which in turn enables the design of tailored coherent control methods that target the specific environmental noise. This is particularly useful to fields such as magnetic imaging and sensing, which tend to operate in the large-error limit and are noise limited. This technique can also bring clarity to the origin of the noise itself. Although speculative, we note for further study that the PSD power law obtained experimentally by the CPMG technique, when extended to higher frequencies, falls within a factor of two of the measured transverse noise, suggesting the possibility that the microscopic mechanism responsible for low-frequency dephasing may also play a role in high-frequency relaxation. In the low-error limit, integrating optimized refocusing pulses into qubit control sequences, for example, by forming composite gates that incorporate both quantum operations and refocusing pulses, may lead to lower net error rates in systems limited by dephasing[38]. Despite observing levels of $1/f$ flux and critical-current noise similar to those observed ubiquitously in superconducting qubits and SQUIDs[21,39], we could mitigate this noise dynamically to increase the pure dephasing times T_φ beyond 0.1 ms, more than a factor of 10^4 longer than the intrinsic pulse length. However, despite having a remarkably long energy-relaxation time $T_1 = 12\,\mu s$, the transverse relaxation $T_2 \approx 2T_1$ was ultimately limited by it. Dynamical-decoupling protocols go a long way to refocusing existing levels of $1/f$ noise and achieve long coherence times, and the main emphasis is now on identifying and mitigating the noise source(s) that cause energy relaxation.

Received 25 February 2011; accepted 4 April 2011; published online 8 May 2011

References

1. Hahn, E. L. Spin echoes. *Phys. Rev.* **80,** 580–594 (1950).
2. Carr, H. Y. & Purcell, E. M. Effects of diffusion on free precession in nuclear magnetic resonance experiments. *Phys. Rev.* **94,** 630–638 (1954).
3. Meiboom, S. & Gill, D. Modified spin-echo method for measuring nuclear relaxation times. *Rev. Sci. Instrum.* **29,** 688–691 (1958).
4. Slichter, C. P. *Principles of Nuclear Magnetic Resonance* 3rd edn (Springer, 1990).
5. Biercuk, M. J. *et al.* Optimized dynamical decoupling in a model quantum memory. *Nature* **458,** 996–1000 (2009).
6. Biercuk, M. J. *et al.* Experimental Uhrig dynamical decoupling using trapped ions. *Phys. Rev. A* **79,** 062324 (2009).
7. Sagi, Y., Almog, I. & Davidson, N. Process tomography of dynamical decoupling in a dense cold atomic ensemble. *Phys. Rev. Lett.* **105,** 053201 (2010).
8. Szwer, D. J., Webster, S. C., Steane, A. M. & Lucas, D. M. Keeping a single qubit alive by experimental dynamic decoupling. *J. Phys. B* **44,** 025501 (2011).
9. Du, J. *et al.* Preserving electron spin coherence in solids by optimal dynamical decoupling. *Nature* **461,** 1265–1268 (2009).
10. Barthel, C., Medford, J., Marcus, C. M., Hanson, M. P. & Gossard, A. C. Interlaced dynamical decoupling and coherent operation of a singlet–triplet qubit. *Phys. Rev. Lett.* **105,** 266808 (2010).
11. Bluhm, H. *et al.* Dephasing time of GaAs electron-spin qubits coupled to a nuclear bath exceeding 200 μs. *Nature Phys.* **7,** 109–113 (2011).
12. de Lange, G., Wang, Z. H., Riste, D., Dobrovitski, V. V. & Hanson, R. Universal dynamical decoupling of a single solid-state spin from a spin bath. *Science* **330,** 60–63 (2010).
13. Ryan, C. A., Hodges, J. S. & Cory, D. G. Robust decoupling techniques to extend quantum coherence in diamond. *Phys. Rev. Lett.* **105,** 200402 (2010).
14. Viola, L. & Lloyd, S. Dynamical suppression of decoherence in two-state quantum systems. *Phys. Rev. A* **58,** 2733–2744 (1998).
15. Faoro, L. & Viola, L. Dynamical suppression of $1/f$ noise processes in qubit systems. *Phys. Rev. Lett.* **92,** 117905 (2004).
16. Falci, G., D'Arrigo, A., Mastellone, A. & Paladino, E. Dynamical suppression of telegraph and $1/f$ noise due to quantum bistable fluctuators. *Phys. Rev. A* **70,** 040101 (2004).
17. Uhrig, G. S. Keeping a quantum bit alive by optimized π-pulse sequences. *Phys. Rev. Lett.* **98,** 100504 (2007).
18. Uhrig, G. S. Exact results on dynamical decoupling by π pulses in quantum information processes. *New J. Phys.* **10,** 083024 (2008).
19. Cywiński, L., Lutchyn, R. M., Nave, C. P. & Das Sarma, S. How to enhance dephasing time in superconducting qubits. *Phys. Rev. B* **77,** 174509 (2008).
20. Pasini, S. & Uhrig, G. S. Optimized dynamical decoupling for power-law noise spectra. *Phys. Rev. A* **81,** 012309 (2010).
21. Clarke, J. & Wilhelm, F. K. Superconducting quantum bits. *Nature* **453,** 1031–1042 (2008).
22. Lasic, S., Stepisnik, J. & Mohoric, A. Displacement power spectrum measurement by CPMG in constant gradient. *J. Magn. Reson.* **182,** 208–214 (2006).
23. Jenista, E. R., Stokes, A. M., Branca, R. T. & Warren, W. S. Optimized, unequal pulse spacing in multiple echo sequences improves refocusing in magnetic resonance. *J. Chem. Phys.* **131,** 204510 (2009).
24. Orlando, T. *et al.* Superconducting persistent-current qubit. *Phys. Rev. B* **60,** 15398–15413 (1999).
25. Mooij, J. E. *et al.* Josephson persistent-current qubit. *Science* **285,** 1036–1039 (1999).
26. Astafiev, O., Pashkin, Y. A., Nakamura, Y., Yamamoto, T. & Tsai, J. S. Quantum noise in the Josephson charge qubit. *Phys. Rev. Lett.* **93,** 267007 (2004).
27. Averin, D. V. Quantum computing and quantum measurement with mesoscopic Josephson junctions. *Fortschr. Phys.* **48,** 1055–1074 (2000).
28. Makhlin, Y., Schön, G. & Shnirman, A. Quantum-state engineering with Josephson-junction devices. *Rev. Mod. Phys.* **73,** 357–400 (2001).
29. Ithier, G. *et al.* Decoherence in a superconducting quantum bit circuit. *Phys. Rev. B* **72,** 134519 (2005).
30. Clerk, A. A., Devoret, M. H., Girvin, S. M., Marquardt, F. & Schoelkopf, R. J. Introduction to quantum noise, measurement, and amplification. *Rev. Mod. Phys.* **82,** 1155–1208 (2010).
31. Yoshihara, F., Harrabi, K., Niskanen, A. O., Nakamura, Y. & Tsai, J. S. Decoherence of flux qubits due to $1/f$ flux noise. *Phys. Rev. Lett.* **97,** 167001 (2006).
32. Martinis, J. M., Nam, S., Aumentado, J., Lang, K. M. & Urbina, C. Decoherence of a superconducting qubit due to bias noise. *Phys. Rev. B* **67,** 094510 (2003).
33. Borneman, T. W., Hurlimann, M. D. & Cory, D. G. Application of optimal control to CPMG refocusing pulse design. *J. Magn. Reson.* **207,** 220–233 (2010).
34. Wellstood, F. C., Urbina, C. & Clarke, J. Low-frequency noise in dc superconducting quantum interference devices below 1 K. *Appl. Phys. Lett.* **50,** 772–774 (1987).
35. Geva, E., Kosloff, R. & Skinner, J. L. On the relaxation of a two-level system driven by a strong electromagnetic field. *J. Chem. Phys.* **102,** 8541–8561 (1995).
36. Van der Wal, C. H., Wilhelm, F. K., Harmans, C. J. P. M. & Mooij, J. E. Engineering decoherence in Josephson persistent-current qubits. *Eur. Phys. J. B* **31,** 111–123 (2003).
37. Shnirman, A., Schön, G., Martin, I. & Makhlin, Y. Low- and high-frequency noise from coherent two-level systems. *Phys. Rev. Lett.* **94,** 127002 (2005).
38. Kerman, A. J. & Oliver, W. D. High-fidelity quantum operations on superconducting qubits in the presence of noise. *Phys. Rev. Lett.* **101,** 070501 (2008).
39. Van Harlingen, D. J. *et al.* Decoherence in Josephson-junction qubits due to critical-current fluctuations. *Phys. Rev. B* **70,** 064517 (2004).

Acknowledgements

We gratefully acknowledge T. Orlando for support in all aspects of this work. We appreciate M. Biercuk, J. Clarke, L. Levitov and S. Lloyd for discussions, and P. Forn-Diaz and S. Valenzuela for comments on the manuscript. We thank P. Murphy and the LTSE team at MIT Lincoln Laboratory for technical assistance. This work was sponsored by the US Government, the Laboratory for Physical Sciences, the National Science Foundation and the Funding Program for World-Leading Innovative R&D on Science and Technology (FIRST), CREST-JST, MEXT kakenhi 'Quantum Cybernetics'. Opinions, interpretations, conclusions and recommendations are those of the author(s) and are not necessarily endorsed by the US Government.

Author contributions

F. Yoshihara, K.H., Y.N. and J-S.T. designed and fabricated the device. J.B. and S.G. carried out the experiments. G.F., S.G. and J.B. contributed to the software infrastructure. J.B., F. Yan, W.D.O. and Y.N. analysed the data and F. Yoshihara and D.G.C. provided feedback. J.B. and W.D.O. wrote the paper with feedback from all authors. W.D.O. supervised the project. All authors contributed to discussions during the conception, execution and interpretation of the experiments.

Additional information

The authors declare no competing financial interests. Supplementary information accompanies this paper on www.nature.com/naturephysics. Reprints and permissions information is available online at http://www.nature.com/reprints. Correspondence and requests for materials should be addressed to J.B.